nature COMMUNICATIONS

ARTICLE

https://doi.org/10.1038/s41467-020-15043-z OPEN

Oxide-ion conduction in the Dion–Jacobson phase $CsBi_2Ti_2NbO_{10-\delta}$

Wenrui Zhang [1], Kotaro Fujii [1], Eiki Niwa [1], Masato Hagihala [2], Takashi Kamiyama [2] & Masatomo Yashima [1✉]

Oxide-ion conductors have found applications in various electrochemical devices, such as solid-oxide fuel cells, gas sensors, and separation membranes. Dion–Jacobson phases are known for their rich magnetic and electrical properties; however, there have been no reports on oxide-ion conduction in this family of materials. Here, for the first time to the best of our knowledge, we show the observation of fast oxygen anionic conducting behavior in $CsBi_2Ti_2NbO_{10-\delta}$. The bulk ionic conductivity of this Dion–Jacobson phase is 8.9×10^{-2} S cm^{-1} at 1073 K, a level that is higher than that of the conventional yttria-stabilized zirconia. The oxygen ion transport is attributable to the large anisotropic thermal motions of oxygen atoms, the presence of oxygen vacancies, and the formation of oxide-ion conducting layers in the crystal structure. The present finding of high oxide-ion conductivity in rare-earth-free $CsBi_2Ti_2NbO_{10-\delta}$ suggests the potential of Dion–Jacobson phases as a platform to identify superior oxide-ion conductors.

[1] Department of Chemistry, School of Science, Tokyo Institute of Technology, 2-12-1 W4-17 O-okayama, Meguro-ku, Tokyo 152-8551, Japan. [2] Institute of Materials Structure Science, High Energy Accelerator Research Organization (KEK), 203-1 Tokai, Ibaraki 319-1106, Japan. ✉email: yashima@cms.titech.ac.jp

Oxide-ion conductors have attracted much attention because of their extensive applications, including in solid-oxide fuel cells, gas sensors, oxygen separation membranes, and catalysts[1–9]. Due to the interaction of oxide ions with the cation network, high oxide-ion conductivities have been achieved in a limited number of structure families; for example, the fluorite-type, perovskite-type, melilite-type, and apatite-type structures[10–17]. Since the limited structure families restrict further development in chemistry and solid-state ionics, the discovery of oxide-ion conductors with new crystal structures is of vital importance for the development of their applications. Various layered perovskites such as BIMEVOX[18–21], the Aurivillius phase[22–24], the Ruddlesden–Popper phase[14,15,25–29], the double perovskites[30–32], the brownmillerites[33,34], the hexagonal perovskite derivative ($Ba_3MoNbO_{8.5}$)[35–37], and the $BaNdInO_4$-based oxides[16,38–40] were reported to exhibit high oxide-ion conductivities. The Dion–Jacobson phase is an A'/A cation-ordered layered perovskite with a general formula of A' $[A_{n-1}B_nO_{3n+1}]$ (A' = Cs, Rb, Li, H, Ag; A = La, Ca, Sr, Bi; and B = Ti, Nb, Ta, etc.), where n denotes the number of the BO_6 octahedral layers, and the A' cation separates the $A_{n-1}B_nO_{3n+1}$ perovskite-like layers[41,42]. Thus, oxide-ion conduction can be expected in the Dion–Jacobson phases. Numerous studies have been conducted on the electrical properties of the Dion–Jacobson phases, such as ferroelectricity[43], proton[44,45], lithium-ion[46,47], sodium-ion[47,48], and mixed proton–electron conduction[49]. However, there are no reports on oxide-ion conduction in the Dion–Jacobson phases. Herein, we report oxide-ion conduction in the Dion–Jacobson phase for the first time.

Here, we have screened 69 Dion–Jacobson phases using available crystallographic data and the bond-valence method (see the details in Supplementary Methods, Supplementary Fig. 1 and Supplementary Table 1)[12,13,16,17,37,38,40,50–53]. The chemical composition of $CsBi_2Ti_2NbO_{10}$ is selected because the bond-valence-based energy barrier for the oxide-ion migration, E_b, is relatively low (E_b = 0.5 eV) and $CsBi_2Ti_2NbO_{10}$ does not contain expensive rare-earth elements. Surprisingly, it is found that the bulk conductivities (σ_b) of the Dion–Jacobson phase of $CsBi_2Ti_2NbO_{10-\delta}$ are as high as 8.9×10^{-2} S cm^{-1} at 1073 K and 1.5×10^{-2} S cm^{-1} at 873 K, which are higher than those of the conventional yttria-stabilized zirconia (YSZ). In consideration of the wide compositional space in Dion–Jacobson phases A' $[A_{n-1}B_nO_{3n+1}]$ (where A' = Cs, Rb, Li, H, Ag; A = La, Ca, Sr, Bi; B = Ti, Nb, Ta, etc., and n ranges from 2 to 6, and examples are presented in Supplementary Table 1), the present discovery provides new possibilities in the chemistry of oxide-ion conductors.

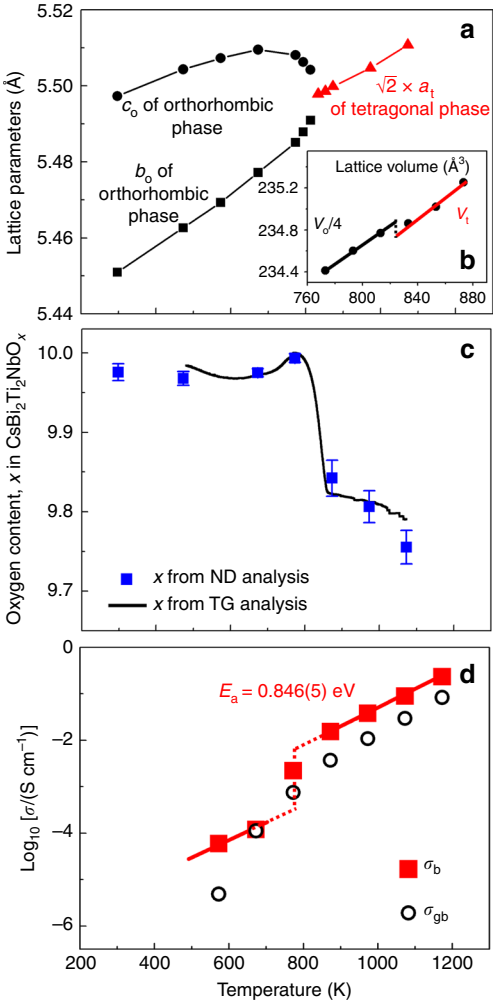

Fig. 1 Temperature dependences of lattice parameters, oxygen content, and conductivities. Lattice parameters (**a**) and reduced lattice volume (**b**) of $CsBi_2Ti_2NbO_{10-\delta}$, which were refined using synchrotron X-ray powder diffraction data measured in situ at high temperatures in static air on heating. The subscripts o and t denote orthorhombic and tetragonal, respectively. **c** Oxygen contents of $CsBi_2Ti_2NbO_{10-\delta}$ on heating, which were obtained by thermogravimetric (TG) analysis in dry air (black line) and calculated from occupancy factors refined using in situ neutron-diffraction (ND) data in vacuum (blue marks). **d** Bulk electrical conductivity σ_b and grain boundary conductivity σ_{gb} of $CsBi_2Ti_2NbO_{10-\delta}$ in dry air on heating.

Results

Phase transition and oxygen content of $CsBi_2Ti_2NbO_{10-\delta}$. $CsBi_2Ti_2NbO_{10-\delta}$ was synthesized by the solid-state reactions. The Rietveld refinements of the synchrotron X-ray diffraction data taken in static air and neutron-diffraction data obtained in vacuum were successfully performed using a single orthorhombic *Ima*2 structure at 297–813 K and a single tetragonal *P*4/*mmm* structure at 833–1073 K on heating (Fig. 1a, Supplementary Figs. 2, 3a, 4a, 5, and Supplementary Tables 2 and 3). The 002 and 020 peaks and 602 and 620 ones of the orthorhombic phase approached each other and merged at a temperature between 813 and 833 K on heating (Supplementary Fig. 4a). The *b*- and *c*-axis lengths of the orthorhombic phase continuously approached each other, leading to thermal expansion anomalies (Supplementary Fig. 6), and coincided at a temperature between 813 and 833 K on heating (Fig. 1a and Supplementary Fig. 3b). These results indicate that the orthorhombic-to-tetragonal (o-to-t) phase transition occurred at a temperature between 813 and 833 K on heating, which is consistent with the literature[43]. The reversible t-to-o transition was observed at a temperature between 793 and 813 K on cooling (Supplementary Fig. 4b), exhibiting a hysteresis of about 20 K. In addition, the reduced lattice volume of $CsBi_2Ti_2NbO_{10-\delta}$ discontinuously decreased between the orthorhombic and tetragonal phases (the lattice volume change is −0.042 (5)%) (Fig. 1b). The hysteresis and discontinuous decrease indicate that the o-t phase transition is first order. It was found that the o-to-t transition was accompanied by 0.32 wt% weight loss on heating, as shown in the thermogravimetric (TG) results (black line in Fig. 1c). The weight loss was caused by an increase in the oxygen vacancy concentration (blue squares in Fig. 1c). The presence of oxygen vacancies (δ) in the high-temperature tetragonal phase of $CsBi_2Ti_2NbO_{10-\delta}$ was confirmed by both the oxygen occupancy factors refined using variable temperature neutron-diffraction data and oxygen contents estimated by the

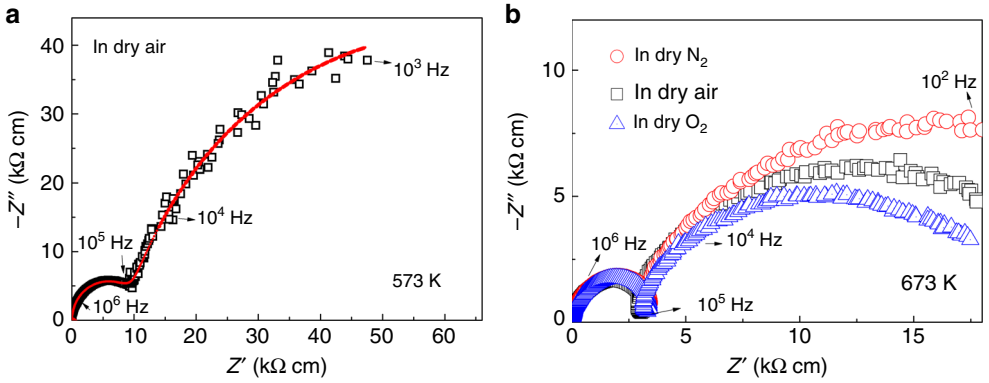

Fig. 2 Complex impedance plots of $CsBi_2Ti_2NbO_{10-\delta}$. **a** Complex impedance plots recorded in flowing dry air at 573 K on heating. Red line indicates the equivalent circuit fitting. The equivalent circuit used to model the impedance data and complex impedance plots at different temperatures are shown in Supplementary Fig. 7. **b** Complex impedance plots measured in flowing dry N_2, air, and O_2 gases at 673 K on heating.

TG analysis (Fig. 1c). The oxygen vacancies are responsible for the high oxide-ion conductivities described later in this paper.

Oxide-ion conduction of $CsBi_2Ti_2NbO_{10-\delta}$. The electrical conductivities of $CsBi_2Ti_2NbO_{10-\delta}$ were measured from 573 to 1173 K using AC and DC methods. Figure 2 shows the typical impedance spectra of $CsBi_2Ti_2NbO_{10-\delta}$. The bulk and grain boundary responses were observed [respective capacitance values of $C_b \approx 0.7 \times 10^{-12}$ F cm^{-1} and $C_{gb} \approx 7.0 \times 10^{-9}$ F cm^{-1} at 573 K in dry air (Fig. 2a)]. The bulk conductivities (σ_b) were independent of the oxygen partial pressure (dry O_2, dry air, and dry N_2; Fig. 2b), which indicates ionic conduction in $CsBi_2Ti_2NbO_{10-\delta}$. Figure 1d shows the temperature dependence of the σ_b and grain boundary conductivities (σ_{gb}) of $CsBi_2Ti_2NbO_{10-\delta}$ on heating. The σ_b abruptly increased between 673 and 873 K on heating, which was attributed to the increase in the carrier (oxygen vacancy) concentration (Fig. 1c) and the o-to-t phase transition (Fig. 1a, b). The total DC electrical conductivity also exhibited an abrupt increase around the o-to-t transition point on heating (Supplementary Fig. 8).

Oxygen concentration cell measurements were performed to determine the oxide-ion transport number (t_{ion}). The t_{ion} values were 1.00–0.98 between 873 and 1173 K in air/O_2, 0.97–0.95 between 873 and 1173 K in air/N_2, and 0.87 at 873 K in air/5% H_2 in N_2 (Fig. 3a). The total DC electrical conductivity (σ_{tot}) at 973 K was almost independent of the oxygen partial pressure $P(O_2)$ between $P(O_2) = 2.0 \times 10^{-22}$ and 1 atm (Fig. 3b). At the $P(O_2) < 2.0 \times 10^{-22}$ region, an n-type electronic contribution to the total conductivity was observed, which is consistent with the relatively low t_{ion} in air/5% H_2 in N_2. The electronic conduction is attributable to the formation of oxygen vacancies and electronic defects accompanied by reduction of Ti^{4+} and/or Nb^{5+} cations in the reducing atmosphere. No significant proton conduction was observed between 873 and 1173 K because the conductivities measured in dry air (H_2O partial pressure, $P(H_2O) < 1.8 \times 10^{-4}$ atm) agreed well with those in wet air ($P(H_2O) = 2.3 \times 10^{-2}$ atm) (Fig. 3c). These results indicate that the oxide ion is the dominant carrier and that $CsBi_2Ti_2NbO_{10-\delta}$ is an oxide-ion conductor. No change was observed in the X-ray powder diffraction patterns before and after the impedance spectroscopy and oxygen concentration cell measurements (Supplementary Fig. 9), which demonstrated the high phase stability of $CsBi_2Ti_2NbO_{10-\delta}$ at high temperatures and different $P(O_2)$ values. The σ_b of $CsBi_2Ti_2NbO_{10-\delta}$ was higher than that of YSZ and comparable with those of the best oxide-ion conductors (Fig. 3d). This indicates the high potential of the Dion–Jacobson phase $CsBi_2Ti_2NbO_{10-\delta}$ as a basic composition for oxide-ion conductors.

Structural origin of the high oxide-ion conductivity of $CsBi_2Ti_2NbO_{10-\delta}$. Next, we discuss the structural origin of the high oxide-ion conductivity using the crystal structure of tetragonal $CsBi_2Ti_2NbO_{9.80(2)}$ at 973 K (Fig. 4). This structure was obtained by the Rietveld refinement of the neutron-diffraction data measured in situ at 973 K with a super-high-resolution diffractometer, SuperHRPD[58,59]. The tetragonal structure of $CsBi_2Ti_2NbO_{10-\delta}$ consists of an oxide-ion conducting inner perovskite Bi-$(Ti_{0.804}Nb_{0.196})O_{3-3\delta/10}$ layer, two outer perovskite Bi-$(Ti_{0.598}Nb_{0.402})O_{3-3\delta/10}$ layers, and an insulating $CsO_{1-\delta/10}$ rock-salt layer (Fig. 4a and Supplementary Fig. 5). The refined equivalent isotropic atomic displacement parameters of the equatorial oxygen atom, O1, (U_{eq}(O1)) and apical oxygen, O2, (U_{eq}(O2)) in the oxide-ion conducting inner perovskite layer were much higher than those of the equatorial O3 and apical O4 atoms in the outer perovskite layers (U_{eq}(O1) = 0.0879(9) Å^2, U_{eq}(O2) = 0.0734(8) Å^2 >> U_{eq}(O3) = 0.0441(5) Å^2, U_{eq}(O4) = 0.0382(5) Å^2). The higher atomic displacement parameters of O1 and O2 were consistent with the results in the literature[43] and from the synchrotron X-ray diffraction data (Supplementary Table 4). Therefore, the O1 and O2 atoms in the inner oxide-ion conducting perovskite layer exhibited larger thermal motions than the O3 and O4 atoms in the outer perovskite layer. In particular, the anisotropic atomic displacement parameters (U_{ij}) of the O1 and O2 atoms were extremely large: U_{11}(O1) = 0.0901(19) Å^2, U_{33}(O1) = 0.157(3) Å^2, and U_{11}(O2) = U_{22}(O2) = 0.1010(11) Å^2 (see others in Supplementary Table 3). The large U_{33}(O1) and U_{11}(O2) values indicate high anisotropic thermal motions along the *c* and *a* axes, respectively, which suggests the O1–O2 oxide-ion diffusion (blue-dotted arrows in Fig. 4a). Similarly, the large U_{11}(O1) means that there are high thermal motions along the *a* and *b* axes, indicating the O1–O1 oxide-ion diffusion (the red-dotted arrows in Fig. 4d). The isosurfaces of the neutron scattering length density obtained by the maximum-entropy method (MEM)[11,12,14,15,31,37,60,61] (yellow isosurfaces in Fig. 4b, e) and bond-valence-based energy landscapes (BVELs, blue isosurfaces in Supplementary Fig. 10) also showed anisotropic thermal motions of O1 and O2 atoms. The O1–O2 and O1–O1 oxide-ion diffusion paths were clearly observed in the BVELs (dotted arrows in Fig. 4c, f). In addition, the O2–O3 diffusion path was observed in the BVELs (the black dotted arrows in Fig. 4c). These results indicate two-dimensional (2D) oxide-ion diffusion along the edges of the Bi$(Ti_{0.804}Nb_{0.196})O_{3-3\delta/10}$ octahedron in the oxide-ion conducting inner perovskite layer. We attribute the high oxide-ion conductivity of $CsBi_2Ti_2NbO_{10-\delta}$ not only to the existence of oxygen vacancies but also to the 2D oxide-ion diffusion and the extremely high U_{eq}(O1), U_{eq}(O2), U_{11}(O1), U_{33}(O1), and

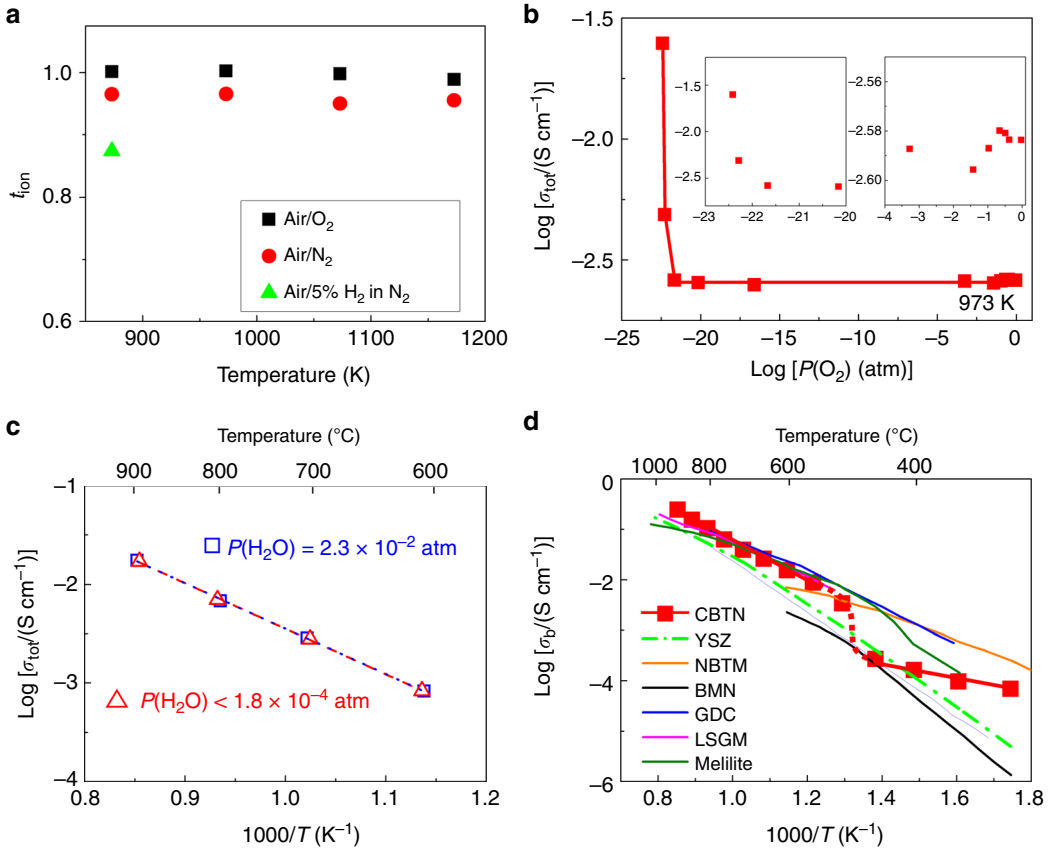

Fig. 3 Oxide-ion conduction of $CsBi_2Ti_2NbO_{10-\delta}$. **a** Oxide-ion transport number t_{ion} determined by oxygen concentration cell measurements of $CsBi_2Ti_2NbO_{10-\delta}$. **b** Partial oxygen pressure $P(O_2)$ dependence of total DC electrical conductivities σ_{tot} of $CsBi_2Ti_2NbO_{10-\delta}$ at 973 K and the insets show the zoom-in view of high and low $P(O_2)$ regions. **c** Arrhenius plots of σ_{tot} of $CsBi_2Ti_2NbO_{10-\delta}$ in dry and wet air. **d** Comparison of bulk conductivity σ_b of $CsBi_2Ti_2NbO_{10-\delta}$ (CBTN) on cooling with those of best oxide-ion conductors: $(Y_2O_3)_{0.08}(ZrO_2)_{0.92}$ (YSZ)[54], $Na_{0.5}Bi_{0.49}Ti_{0.98}Mg_{0.02}O_{2.965}$ (NBTM)[55], $Ba_3MoNbO_{8.5}$ (BMN)[36], $Ce_{0.9}Gd_{0.1}O_{1.95}$ (GDC)[56], $La_{0.9}Sr_{0.1}Ga_{0.8}Mg_{0.2}O_{2.85}$ (LSGM)[6], and $La_{1.54}Sr_{0.46}Ga_3O_{7.27}$ (melilite)[57].

U_{11}(O2) [=U_{22}(O2)]. In fact, these thermal parameters of $CsBi_2Ti_2NbO_{10-\delta}$ are much higher than those of perovskite-type and layered perovskite-type conductors, such as $La_{0.9}Sr_{0.1}Ga_{0.79}Mg_{0.21}O_{2.82}$[62], $La_{0.8}Sr_{0.2}Ga_{0.8}Mg_{0.15}Co_{0.05}O_{2.8}$[63], $BaBi_4Ti_4O_{15}$[23], $Bi_4Ti_3O_{12}$[64], and $Bi_2Sr_2TiNb_2O_{12}$[65] (Supplementary Tables 5 and 6).

Discussion

Here, we propose a new concept: large bottlenecks for oxide-ion migration by the large size of Cs^+ and Bi^{3+} displacement. The bottlenecks of $CsBi_2Ti_2NbO_{10-\delta}$ are the Bi–Bi–Ti triangles (the yellow and pink triangles in Fig. 5a–c). The large bottlenecks of $CsBi_2Ti_2NbO_{10-\delta}$ can be explained using the new concept, as described below. Cs^+ expands the Bi–Bi distance along the b axis (the orange arrows in Fig. 5a) due to the occupational ordering of the large Cs^+ and small Bi^{3+} cations. Bi^{3+} is displaced along the c axis apart from the Ti/Nb1–O1 layer (the blue arrows in Fig. 5a), by electrostatic forces (Supplementary Note 1 and Supplementary Fig. 11). The Bi^{3+} displacement increases the Bi–Bi distance along the c axis. The increase in the Bi–Bi distances along both the b (=a) and c axes leads to large bottlenecks for the O1–O2 (the yellow areas) and O1–O1 (the pink areas) oxide-ion diffusion (Fig. 5b–d). Since the bottleneck of $CsBi_2Ti_2NbO_{10-\delta}$ is the Bi–Bi–Ti triangle, it is interesting to compare the bottleneck sizes (critical radii) and oxide-ion conductivities of $CsBi_2Ti_2NbO_{10-\delta}$ with those of layered perovskites with Bi–Bi–Ti bottleneck triangles, $BaBi_4Ti_4O_{15}$, $Bi_4Ti_3O_{12}$, and $Bi_2Sr_2TiNb_2O_{12}$. The oxide-ion conductivity of $CsBi_2Ti_2NbO_{10-\delta}$ was much higher than those of these materials, which is attributable to the larger bottlenecks (Supplementary Table 7).

In summary, we have discovered the first example of the Dion–Jacobson-type oxide-ion conductor ($CsBi_2Ti_2NbO_{10-\delta}$). It was found that $CsBi_2Ti_2NbO_{10-\delta}$ exhibits a high σ_b of 8.9 × 10^{-2} S cm^{-1} at 1073 K and high phase stability at high temperatures and different $P(O_2)$ values. The conductivity abruptly increased between 673 and 873 K on heating, which is ascribed to the increase in oxygen vacancy concentration and the o-to-t phase transition. The high oxide-ion conductivities of Cs/Bi-cation-ordered $CsBi_2Ti_2NbO_{10-\delta}$ are attributable to (i) the large anisotropic thermal motions of the oxygen atoms in the inner oxide-ion conducting perovskite layer, (ii) the 2D O1–O2 and O1–O1 oxide-ion diffusion, (iii) the existence of oxygen vacancies and (iv) the large bottlenecks. We have also proposed a concept: large bottlenecks for oxide-ion migration by large size of Cs^+ and Bi^{3+} displacement. The oxide-ion conductivity is expected to be improved by doping and/or modification of the chemical composition of the basic material $CsBi_2Ti_2NbO_{10-\delta}$. The present finding of high oxide-ion conductivities in the new structure family, Dion–Jacobson-type $CsBi_2Ti_2NbO_{10-\delta}$, and the concept would facilitate the design of novel oxide-ion conductors based on the Dion–Jacobson phases.

Methods

Synthesis and characterization of $CsBi_2Ti_2NbO_{10-\delta}$. $CsBi_2Ti_2NbO_{10-\delta}$ was synthesized by the solid-state-reaction method. High-purity (>99.9%) Cs_2CO_3, Bi_2O_3, TiO_2, and Nb_2O_5 (with molar ratios of Cs, Bi, Ti, and Nb = 1.3: 2.0: 2.0: 1.0)

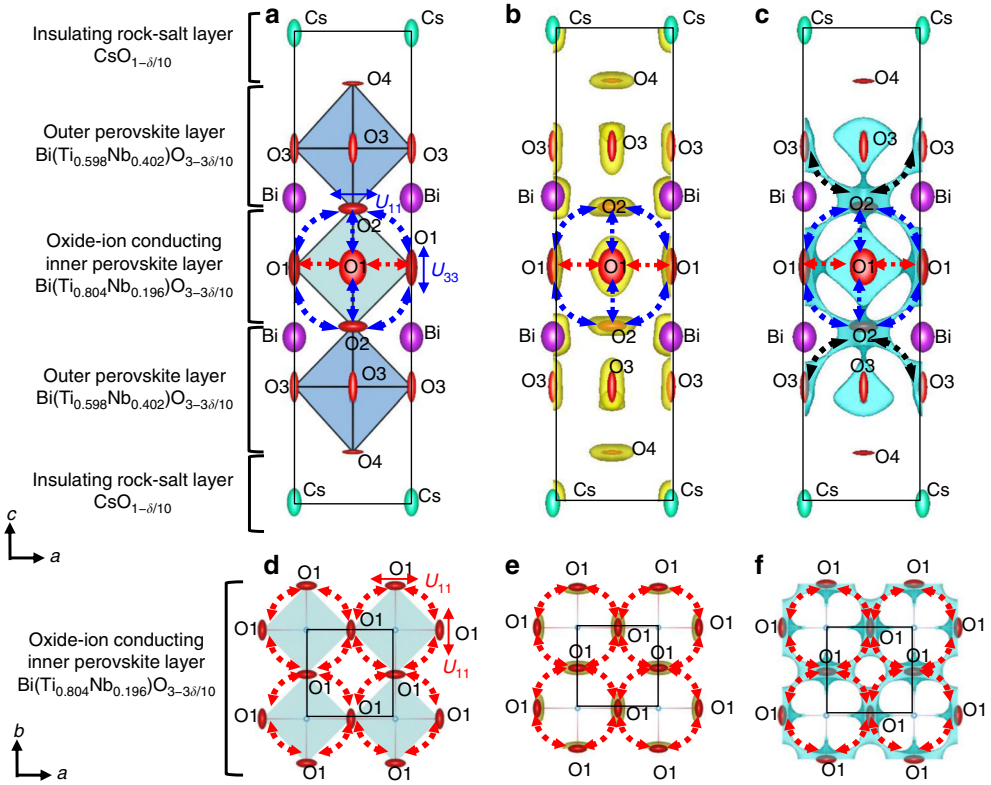

Fig. 4 Crystal structure and oxide-ion diffusion pathway of tetragonal $CsBi_2Ti_2NbO_{9.80(2)}$ at 973 K. a, **d** Refined crystal structure of $CsBi_2Ti_2NbO_{9.80(2)}$ at 973 K, which was obtained by Rietveld analysis of in situ neutron-diffraction data. **b**, **e** Yellow isosurfaces of the neutron scattering length density at 1.0 fm $Å^{-3}$ with the structure (973 K). **c**, **f** Blue isosurfaces of the bond-valence-based energy for an oxide ion at 0.6 eV for the structure at 973 K. Blue, red, and black dotted lines with arrows denote the possible O1–O2, O1–O1, and O2–O3 diffusion pathways of oxide ion, respectively. The solid lines with arrows in **a** and **d** stand for the directions of anisotropic thermal motions of O1 and O2 oxygen atoms. Thermal ellipsoids are drawn at the 50% probability level. Regions of **a**–**c** $-1/2 \le x, y, z \le 1/2$ and of **d**–**f** $-1/2 \le x, y \le 3/2$, $0 \le z \le 0.1$.

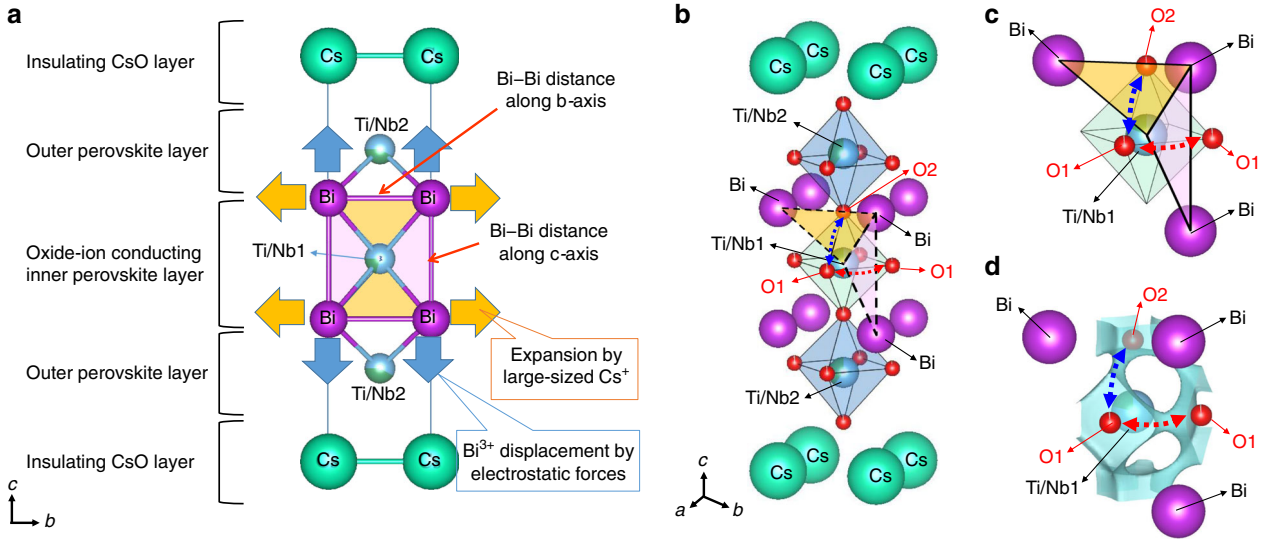

Fig. 5 New concept of enlarged bottlenecks for oxide-ion migration by large size of Cs^+ and Bi^{3+} displacement. a New concept of enlarged bottlenecks for oxide-ion migration created by large size of Cs^+ and Bi^{3+} displacement in Dion–Jacobson-type Cs/Bi-cation-ordered $CsBi_2Ti_2NbO_{10-\delta}$ ($-1/2 \le x, y, z \le 1/2$). Yellow and pink Bi–Bi–Ti triangles stand for the areas of bottlenecks for O1–O2 and O1–O1 oxide-ion migration, respectively. Oxygen atoms are omitted for simplicity in **a**. **b** Refined structure and Bi–Bi–Ti/Nb1 triangle bottleneck of $CsBi_2Ti_2NbO_{9.80(2)}$ at 973 K ($-1/2 \le x, y, z \le 1/2$). A part of the structure (**c**) and corresponding bond-valence-based energy landscape (BVEL) with the isosurface at 0.6 eV (**d**), showing the O1–O2 and O1–O1 oxide-ion diffusion paths. Blue and red-dotted lines with arrows denote the possible O1–O2 and O1–O1 diffusion pathways of oxide ion, respectively.

were mixed and ground using an agate mortar and a pestle for 30 min as ethanol slurries, where an excess amount of Cs_2CO_3 (30 mol%) was added to compensate for the mass loss due to the volatilisation of the Cs species during sintering[43]. The mixture was dried on a hot plate (with a setting temperature of 373 K) and then ground into powder in the mortar for 30 min. This mixing, drying, and grinding processes were repeated a few times. The obtained mixtures were uniaxially pressed into pellets at about 100 MPa and subsequently sintered in static air at 1173 K for 12 h at heating and cooling rates of 5 K min^{-1}. The grinding, pressing, and sintering processes were repeated a few times until a single phase of $CsBi_2Ti_2NbO_{10-\delta}$ was obtained. Parts of the sintered pellets were crushed and ground into powders to carry out X-ray powder diffraction, synchrotron X-ray powder diffraction, atomic absorption spectroscopy (AAS, Hitachi Z-2300), inductively coupled plasma optical emission spectroscopy (ICP-OES, Hitachi PS3520UVDD), and TG measurements. The existing phase of $CsBi_2Ti_2NbO_{10-\delta}$ was examined with an X-ray powder diffractometer (RINT-2550, Cu $K\alpha$ radiation, 2θ range: 5–100°, Step interval: 0.02°). The AAS and ICP-OES results indicated that the cation molar ratios of $CsBi_2Ti_2NbO_{10-\delta}$ were Cs: Bi: Ti: Nb = 1: 2: 2: 1, which were consistent with the nominal composition. TG analysis was carried out in flowing dry and static air between 297 and 1073 K using a Bruker-AXS 2020SA instrument at heating and cooling rates of 1 K min^{-1}. The measurements between 473 and 1073 K were repeated three times to negate the influence of absorbed species, such as water, and also to confirm the reproducibility. The TG data on the third heating in dry air were plotted in Fig. 1c. The TG data in dry air agreed well with those in static air. The sample did not decompose during the TG measurements, which was confirmed by X-ray powder diffraction measurements of the sample after the TG measurements.

Structure analyses by high-temperature synchrotron X-ray and neutron diffraction. High-angular-resolution SXRPD data of $CsBi_2Ti_2NbO_{10-\delta}$ were obtained in static air between 297 and 1073 K, using six 1D solid-state detectors at the BL02B2 beamline of SPring-8, Japan[66,67]. A powdered sample of $CsBi_2Ti_2NbO_{10-\delta}$ was loaded into a quartz glass capillary with an inner diameter of 0.1 mm for the SXRPD measurements. The wavelength was determined to be 0.6992620(4) Å using silicon powder (NIST SRM 640c). The absorption correction was performed through the empirical formula given by Rouse and Cooper[68].

High-temperature neutron-diffraction measurements were carried out in vacuum using a super-high-resolution time-of-flight neutron diffractometer (SuperHRPD) installed at the Materials and Life Science Experimental Facility of J-PARC, Japan[58,59]. The absorption correction was performed using the method given by Rouse and Cooper[68]. The diffraction data were analysed by the Rietveld method using the Z-Rietveld program[69]. Oxygen contents were calculated using the oxygen occupancy factors refined in the Rietveld analyses of the neutron-diffraction data. The calculated oxygen contents $10-\delta$ in $CsBi_2Ti_2NbO_{10-\delta}$ were 9.84(2) at 873 K, 9.80(2) at 973 K, and 9.76(2) at 1073 K, which were consistent with the TG data: 9.839 at 873 K, 9.828 at 973 K, and 9.807 at 1073 K (Fig. 1c).

The neutron scattering length density distribution was investigated using the MEM. The MEM analysis was carried out with computer program, Dysnomia[70], using the structure factors obtained in the Rietveld refinement of the neutron-diffraction data at 973 K. The MEM calculations were performed with the unit cell divided into $38 \times 38 \times 156$ pixels. The refined crystal structure, MEM neutron scattering length density distributions, and bond-valence-based energy landscape were depicted by VESTA[71].

Conductivity measurements and oxygen concentration cell measurements. The electrical conductivities of $CsBi_2Ti_2NbO_{10-\delta}$ were measured by AC impedance spectroscopy in flowing dry air, N_2, and O_2 gases using a sintered pellet (20 mm in diameter, 2.6 mm in thickness, relative density of 91%) with Au electrodes in the temperature range of 573–1173 K on heating and cooling. The surface of the pellet was polished before smearing Au paste to decrease the electrode resistance. Impedance spectra were recorded with a Solartron 1260 impedance analyzer in the frequency range of 15 MHz–1 Hz at an applied alternating voltage of 100 mV. The bulk and grain boundary responses were evidenced, and equivalent circuit analyses were carried out to extract the σ_b and σ_{gb} at each temperature using the ZView software (Scribner Associates, Inc.). The temperature dependence of σ_{tot} of $CsBi_2Ti_2NbO_{10-\delta}$ was also measured in dry and wet air on cooling by a DC-4-probe method (4.5 mm in diameter, 11 mm in height, and relative density of 91%). The $P(O_2)$ dependence of the σ_{tot} was measured at 973 K in the $P(O_2)$ region between 3×10^{-23} and 1 atm using a mixture of O_2, N_2, and 5% H_2 in N_2 by the DC 4-probe method (4.6 mm in diameter, 12 mm in height, and relative density of 88%). $P(O_2)$ was monitored by an oxygen sensor.

Oxygen concentration cell measurements were performed to determine the oxide-ion transport number t_{ion} using a sintered pellet (20 mm in diameter, 4.5 mm in height, and relative density of 91%) attached to an alumina tube with a glass seal. One side of the pellet was exposed to a flowing dry air and the other side to a flowing dry O_2 (Air/O_2), N_2 (Air/N_2), and 5% H_2 in N_2 (Air/5% H_2 in N_2) gases between 873 and 1173 K. The electromotive forces of the concentration cell were measured using a Keithley model 617 electrometer. The following Nernst equation was used to estimate the t_{ion}:

$$E = t_{ion} \frac{RT}{4F} ln\left(\frac{P(O_2)}{P^0(O_2)}\right), \quad (1)$$

where F is the Faraday constant, R is the gas constant, T is the absolute temperature, $P(O_2)$ is the oxygen partial pressure of the gas of O_2, N_2, 5% H_2 in N_2, and $P^0(O_2)$ (=0.21 atm) is the oxygen partial pressure of dry air.

The activation energies, E_a, for the conductivities were estimated using the Arrhenius equation:

$$\sigma = \frac{A_0}{T} \exp\left(-\frac{E_a}{kT}\right), \quad (2)$$

where A_0, k, and T are the pre-exponential factor, Boltzmann constant, and absolute temperature, respectively.

After the impedance spectroscopy and oxygen concentration cell measurements, the surface of the pellet was ground with sandpaper carefully to remove the Au paste and then crushed and ground into powder. The powder was used for the X-ray diffraction measurements to investigate the phase stability at high temperatures and different atmospheres.

Data availability

The data that support the findings of this study are available from the corresponding author upon reasonable request.

Received: 15 October 2019; Accepted: 17 February 2020;
Published online: 06 March 2020

References

1. Malavasi, L., Fisher, C. A. J. & Islam, M. S. Oxide-ion and proton conducting electrolyte materials for clean energy applications: structural and mechanistic features. *Chem. Soc. Rev.* **39**, 4370–4387 (2010).
2. Boivin, J. C. & Mairesse, G. Recent material developments in fast oxide ion conductors. *Chem. Mater.* **10**, 2870–2888 (1998).
3. Goodenough, J. B. Oxide-ion conductors by design. *Nature* **404**, 821–823 (2000).
4. Kharton, V. V., Yaremchenko, A. A., Naumovich, E. N. & Marques, F. M. B. Research on the electrochemistry of oxygen ion conductors in the former Soviet Union. *J. Solid State Electrochem.* **3**, 303–326 (1999).
5. Skinner, S. J. & Kilner, J. A. Oxygen ion conductors. *Mater. Today* **3**, 30–37 (2003).
6. Ishihara, T., Matsuda, H. & Takita, Y. Doped $LaGaO_3$ perovskite type oxide as a new oxide ionic conductor. *J. Am. Chem. Soc.* **116**, 3801–3803 (1994).
7. Ishihara, T., Kilner, J. A., Honda, M. & Takita, Y. Oxygen surface exchange and diffusion in the new perovskite oxide ion conductor $LaGaO_3$. *J. Am. Chem. Soc.* **119**, 2747–2748 (1997).
8. Malavasi, L. et al. Nature of the monoclinic to cubic phase transition in the fast oxygen ion conductor $La_2Mo_2O_9$ (LAMOX). *J. Am. Chem. Soc.* **129**, 6903–6907 (2007).
9. Adachi, G. Y., Imanaka, N. & Tamura, S. Ionic conducting lanthanide oxides. *Chem. Rev.* **102**, 2405–2429 (2002).
10. Lacorre, P., Goutenoire, F., Bohnke, O., Retoux, R. & Laligant, Y. Designing fast oxide-ion conductors based on $La_2Mo_2O_9$. *Nature* **404**, 856–858 (2000).
11. Yashima, M. Diffusion pathway of mobile ions and crystal structure of ionic and mixed conductors—a brief review. *J. Ceram. Soc. Jpn.* **117**, 1055–1059 (2009).
12. Yashima, M. Invited Review: Some recent developments in the atomic-scale characterization of structural and transport properties of ceria-based catalysts and ionic conductors. *Catal. Today* **253**, 3–19 (2015).
13. Fujii, K. & Yashima, M. Discovery and development of $BaNdInO_4$—a brief review. *J. Ceram. Soc. Jpn.* **126**, 852–859 (2018).
14. Yashima, M., Sirikanda, N. & Ishihara, T. Crystal structure, diffusion path and oxygen permeability of a Pr_2NiO_4-based mixed conductor $(Pr_{0.9}La_{0.1})_2(Ni_{0.74}Cu_{0.21}Ga_{0.05})O_{4+\delta}$. *J. Am. Chem. Soc.* **132**, 2385–2392 (2010).
15. Yashima, M. et al. Structural disorder and diffusional pathway of oxide ions in a doped Pr_2NiO_4-based mixed conductor. *J. Am. Chem. Soc.* **130**, 2762–2763 (2008).
16. Fujii, K. et al. New perovskite-related structure family of oxide-ion conducting materials $NdBaInO_4$. *Chem. Mater.* **26**, 2488–2491 (2014).
17. Fujimoto, A., Yashima, M., Fujii, K. & Hester, J. R. New oxide-ion conductor $SrYbInO_4$ with partially cation-disordered $CaFe_2O_4$-type structure. *J. Phys. Chem. C.* **121**, 21272–21280 (2017).
18. Abraham, F., Boivin, J. C., Mairesse, G. & Nowogrocki, G. The BIMEVOX series: a new family of high performances oxide ion conductors. *Solid State Ion.* **40–41**, 934–937 (1990).
19. Iharada, T. et al. Electrochemical characterization of BIMEVOX oxide-ion conductors. *Solid State Ion.* **48**, 257–265 (1991).
20. Pirovano, C., Steil, M. C., Capoen, E., Nowogrocki, G. & Vannier, R. N. Impedance study of the microstructure dependence of the electrical properties of BIMEVOXes. *Solid State Ion.* **176**, 2079–2083 (2005).

21. Lee, C. K. & West, A. R. Thermal behaviour and polymorphism of BIMEVOX oxide ion conductors including the new materials: $Bi_4V_2O_{11}$: M; M= La, Y, Mg, B. *Solid State Ion.* **86-88**, 235–239 (1996).
22. Kendall, K. R., Navas, C., Thomas, J. K. & zur Loye, H.-C. Recent developments in oxide ion conductors: aurivillius phases. *Chem. Mater.* **8**, 642–649 (1996).
23. Thomas, J. K., Anderson, M. E., Krause, W. E. & zur Loye, H.-C. Oxygen ion conductivity in a new class of layered bismuth oxide compounds. *MRS Res. Soc. Symp. Proc.* **293**, 295–300 (1993).
24. Porob, D. G. & Guru Row, T. N. A novel oxide ion conductor in a doped Bi_2O_3-V_2O_5 system: Ab initio structure of a new polymorph of $NaBi_3V_2O_{10}$ via powder X-ray diffraction. *Chem. Mater.* **12**, 3658–3661 (2000).
25. Amow, G. & Skinner, S. J. Recent developments in Ruddlesden–Popper nickelate systems for solid oxide fuel cell cathodes. *J. Solid State Electrochem.* **10**, 538–546 (2006).
26. Patrakeev, M. V., Leonidov, I. A., Kozhevnikov, V. L. & Kharton, V. V. Ion-electron transport in strontium ferrites: Relationships with structural features and stability. *Solid State Sci.* **6**, 907–913 (2004).
27. Yamada, A. et al. Ruddlesden-Popper-type epitaxial film as oxygen electrode for solid-oxide fuel cells. *Adv. Mater.* **20**, 4124–4128 (2008).
28. Yang, G., Su, C., Ran, R., Tade, M. O. & Shao, Z. Advanced symmetric solid oxide fuel cell with an infiltrated K_2NiF_4-Type La_2NiO_4 electrode. *Energy and Fuels* **28**, 356–362 (2014).
29. Ishihara, T., Nakashima, K., Okada, S., Enoki, M. & Matsumoto, H. Defect chemistry and oxygen permeation property of $Pr_2Ni_{0.75}Cu_{0.25}O_4$ oxide doped with Ga. *Solid State Ion.* **179**, 1367–1371 (2008).
30. Sengodan, S. et al. Layered oxygen-deficient double perovskite as an efficient and stable anode for direct hydrocarbon solid oxide fuel cells. *Nat. Mater.* **14**, 205–209 (2014).
31. Ali, R., Yashima, M. & Izumi, F. Diffusion path of oxide ions in an oxide ion conductor $La_{0.64}(Ti_{0.92}Nb_{0.08})O_{2.99}$ with a double perovskite-type structure. *Chem. Mater.* **19**, 3260–3264 (2007).
32. Burriel, M. et al. Anisotropic oxygen ion diffusion in layered $PrBaCo_2O_{5+\delta}$. *Chem. Mater.* **24**, 613–621 (2012).
33. Goodenough, J. B., Ruiz-Diaz, J. E. & Zhen, Y. S. Oxide-ion conduction in $Ba_2In_2O_5$ and $Ba_3In_2MO_8$ (M=Ce, Hf, or Zr). *Solid State Ion.* **44**, 21–31 (1990).
34. Auckett, J. E. et al. Combined experimental and computational study of oxide ion conduction dynamics in $Sr_2Fe_2O_5$ brownmillerite. *Chem. Mater.* **25**, 3080–3087 (2013).
35. Fop, S., McCombie, K. S., Wildman, E. J., Skakle, J. M. S. & Mclaughlin, A. C. Hexagonal perovskite derivatives: a new direction in the design of oxide ion conducting materials. *Chem. Commun.* **55**, 2127–2137 (2019).
36. Fop, S. et al. Oxide ion conductivity in the hexagonal perovskite derivative $Ba_3MoNbO_{8.5}$. *J. Am. Chem. Soc.* **138**, 16764–16769 (2016).
37. Yashima, M. et al. Direct evidence for two-dimensional oxide-ion diffusion in the hexagonal perovskite-related oxide $Ba_3MoNbO_{8.5-\delta}$. *J. Mater. Chem. A* **7**, 13910–13916 (2019).
38. Fujii, K. et al. Improved oxide-ion conductivity of $NdBaInO_4$ by Sr doping. *J. Mater. Chem. A* **3**, 11985–11990 (2015).
39. Yang, X., Liu, S., Lu, F., Xu, J. & Kuang, X. Acceptor doping and oxygen vacancy migration in layered perovskite $NdBaInO_4$-based mixed conductors. *J. Phys. Chem. C.* **120**, 6416–6426 (2016).
40. Shiraiwa, M. et al. Crystal structure and oxide-ion conductivity of $Ba_{1+x}Nd_{1-x}InO_{4-x/2}$. *J. Electrochem. Soc.* **164**, F1392–F1399 (2017).
41. Dion, M., Ganne, M. & Tournoux, M. The new phase families M(I)M2(II) Nb_3O_{10} with perovskite sheets. *Mater. Res. Bull.* **16**, 1429–1435 (1981).
42. Jacobson, A. J., Johnson, J. W. & Lewandowski, J. T. Interlayer chemistry between thick transition-metal oxide layers: synthesis and intercalation reactions of $K[Ca_2Na_{n-3}Nb_nO_{3n+1}]$. *Inorg. Chem.* **24**, 3727–3729 (1985).
43. McCabe, E. E. et al. Proper ferroelectricity in the Dion-Jacobson material $CsBi_2Ti_2NbO_{10}$: experiment and theory. *Chem. Mater.* **27**, 8298–8309 (2015).
44. Goff, R. J. et al. Leakage and proton conductivity in the predicted ferroelectric $CsBiNb_2O_7$. *Chem. Mater.* **21**, 1296–1302 (2009).
45. Draskovic, T. I., Wang, T., Henderson, C. N. & Mallouk, T. E. Protonic and electronic conductivity of the layered perovskite oxides $HCa_2Nb_3O_{10}$ and $Ca_4Nb_6O_{19}$. *Int. J. Hydrog. Energy* **39**, 4576–4580 (2014).
46. Kim, Y. I. & Kim, S. J. Ionic conductivity of Dion-Jacobson type oxide $LiLaTa_2O_7$ and oxynitride $LiLaTa_2O_{6.15}N_{0.57}$ measured by impedance spectroscopy. *Ceram. Int.* **41**, 3318–3323 (2015).
47. Choy, J. H., Kim, J. Y., Kim, S. J., Sohn, J. S. & Han, O. H. New Dion–Jacobsen-type layered perovskite oxyfluorides, $ASrNb_2O_6F$ (A = Li, Na, and Rb). *Chem. Mater.* **13**, 906–912 (2001).
48. Thangadurai, V. & Weppner, W. Determination of the sodium ion transference number of the Dion–Jacobson-type layered provskite $NaCa_2Nb_3O_{10}$ using ac impedance and dc methods. *Chem. Mater.* **14**, 1136–1143 (2002).
49. Thangadurai, V. & Weppner, W. Mixed potential protonic-electronic conductivity in the Dion–Jacobson-type layered perovskites in hydrogen-containing atmosphere and their application in ammonia sensors. *Solid State Ion.* **174**, 175–183 (2004).
50. Avdeev, M., Sale, M., Adams, S. & Rao, R. P. Screening of the alkali-metal ion containing materials from the Inorganic Crystal Structure Database (ICSD) for high ionic conductivity pathways using the bond valence method. *Solid State Ion.* **225**, 43–46 (2012).
51. Nakamura, K., Fujii, K., Niwa, E. & Yashima, M. Crystal structure and electrical conductivity of BaR_2ZnO_5 (R = Sm, Gd, Dy, Ho, and Er)—a new structure family of oxide-ion conductors. *J. Ceram. Soc. Jpn.* **126**, 292–299 (2018).
52. Uno, W. et al. Experimental visualization of oxide-ion diffusion paths in pyrochlore-type $Yb_2Ti_2O_7$. *J. Ceram. Soc. Jpn.* **126**, 341–345 (2018).
53. Adams, S. Relationship between bond valence and bond softness of alkali halides and chalcogenides. *Acta Crystallogr. Sect. B Struct. Sci. Cryst. Eng. Mater.* **57**, 278–287 (2001).
54. Kwon, O. H. & Choi, G. M. Electrical conductivity of thick film YSZ. *Solid State Ion.* **177**, 3057–3062 (2006).
55. Li, M. et al. A family of oxide ion conductors based on the ferroelectric perovskite $Na_{0.5}Bi_{0.5}TiO_3$. *Nat. Mater.* **13**, 31–35 (2014).
56. Huang, K., Feng, M. & Goodenough, J. B. Synthesis and electrical properties of dense $Ce_{0.9}Gd_{0.1}O_{1.95}$ ceramics. *J. Am. Chem. Soc.* **81**, 357–362 (1998).
57. Kuang, X. et al. Interstitial oxide ion conductivity in the layered tetrahedral network melilite structure. *Nat. Mater.* **7**, 498–504 (2008).
58. Torii, S. et al. Super high resolution powder diffractometer at J-PARC. *J. Phys. Soc. Jpn.* **80**, 3–6 (2011).
59. Torii, S. et al. Improvement of instrument devices for super high resolution powder diffractometer at J-PARC. *J. Phys. Conf. Ser.* **502**, 1–5 (2014).
60. Yashima, M., Itoh, M., Inaguma, Y. & Morii, Y. Crystal structure and diffusion path in the fast lithium-ion conductor $La_{0.62}Li_{0.16}TiO_3$. *J. Am. Chem. Soc.* **127**, 3491–3495 (2005).
61. Chen, Y. C., Yashima, M., Peña-Martínez, J. & Kilner, J. A. Experimental visualization of the diffusional pathway of oxide ions in a layered perovskite-type cobaltite $PrBaCo_2O_{5+\delta}$. *Chem. Mater.* **25**, 2638–2641 (2013).
62. Slater, P. R., Irvine, J. T. S., Ishihara, T. & Takita, Y. High-temperature powder neutron diffraction study of the oxide ion conductor $La_{0.9}Sr_{0.1}Ga_{0.8}Mg_{0.2}O_{2.85}$. *J. Solid State Chem.* **143**, 135–143 (1998).
63. Yashima, M. et al. Conduction path and disorder in the fast oxide-ion conductor $(La_{0.8}Sr_{0.2})(Ga_{0.8}Mg_{0.15}Co_{0.05})O_{2.8}$. *Chem. Phys. Lett.* **380**, 391–396 (2003).
64. Long, C., Fan, H., Ren, W. & Zhao, J. Double polarization hysteresis and dramatic influence of small compositional variations on the electrical properties in $Bi_4Ti_3O_{12}$ ceramics. *J. Eur. Ceram. Soc.* **39**, 4103–4112 (2019).
65. Shi, J. Ph. D. *Dissertation, Crystal structure studies, electrical and magnetic properties of 2, 3, 4, 5-layer aurivillius oxides* (Alfred University, Alfred, New York, 2015).
66. Nishibori, E. et al. The large Debye-Scherrer camera installed at SPring-8 BL02B2 for charge density studies. *J. Phys. Chem. Solids* **62**, 2095–2098 (2001).
67. Kawaguchi, S. et al. High-throughput powder diffraction measurement system consisting of multiple MYTHEN detectors at beamline BL02B2 of SPring-8. *Rev. Sci. Instrum.* **88**, 085111 (2017).
68. Rouse, K. D., Cooper, M. J., York, E. J. & Chakera, A. Absorption corrections for neutron diffraction. *Acta Crystallogr. Sect. A Found. Adv.* **26**, 682–691 (1970).
69. Oishi, R. et al. Rietveld analysis software for J-PARC. *Nucl. Instruments Methods Phys. Res. Sect. A Accel. Spectrom. Detect. Assoc. Equip.* **600**, 94–96 (2009).
70. Momma, K., Ikeda, T., Belik, A. A. & Izumi, F. Dysnomia, a computer program for maximum-entropy method (MEM) analysis and its performance in the MEM-based pattern fitting. *Powder Diffr.* **28**, 184–193 (2013).
71. Momma, K. & Izumi, F. VESTA 3 for three-dimensional visualization of crystal, volumetric and morphology data. *J. Appl. Crystallogr.* **44**, 1272–1276 (2011).

Acknowledgements

We thank Dr S. Torii, Dr P. Miao and Dr S. Kawaguchi for the assistance in the neutron and synchrotron X-ray diffraction experiments. We express special thanks to Mr M. Shiraiwa, Miss H. Kandabashi, and Mr. K. Hibino for useful discussion and assistance in the experiments. We acknowledge Daiichi Kigenso Kagaku Kogyo Co., Ltd for the AAS and ICP-OES measurements. The neutron-diffraction measurements were carried out by the project approval (J-PARC MLF Proposal No. 2017A0111 and 2017L1301). The synchrotron experiments were carried out at SPring-8 (Proposal No. 2017A1803, 2017B1265, 2018A1259, 2018B1056, and 2019A1052). This study was partly supported by Grants-in-Aid for Scientific Research (KAKENHI, No. JP15H02291, JP16H00884, JP16H06293, JP16H06440, JP16H06441, JP16H06438, JP16K21724, JP17K17717, JP17H06222, and JP19H00821) from the Ministry of Education, Culture, Sports, Science and Technology of Japan and JSPS Core-to-Core Program, A. Advanced Research Networks (Solid Oxide Interfaces for Faster Ion Transport).

Author contributions

M.Y. and W.Z. designed research. W.Z., K.F., M.H., and T.K. measured the neutron data. W.Z. prepared the samples and measured the X-ray diffraction data, electrical conductivity, TG data and transport number. E.N. advised W.Z. in the oxygen concentration cell measurements. W.Z. analyzed the data and made figures and tables. W.Z. and M.Y. wrote and edited the manuscript and response to the referees' comments. All the authors read the manuscript and gave comments. Funding acquisition and supervision: M.Y. M. Y. created the new concept with W.Z.

Competing interests

The authors declare no competing interests.

Additional information

Supplementary information is available for this paper at https://doi.org/10.1038/s41467-020-15043-z.

Correspondence and requests for materials should be addressed to M.Y.

Peer review information *Nature Communications* thanks the anonymous reviewer(s) for their contribution to the peer review of this work.

Reprints and permission information is available at http://www.nature.com/reprints

Publisher's note Springer Nature remains neutral with regard to jurisdictional claims in published maps and institutional affiliations.